Characterization of spindle pole body duplication reveals a regulatory role for nuclear pore complexes

Diana Rüthnick,[1] Annett Neuner,[1] Franziska Dietrich,[1] Daniel Kirrmaier,[1] Ulrike Engel,[2] Michael Knop,[1] and Elmar Schiebel[1]

[1]Zentrum für Molekulare Biologie at the University of Heidelberg, German Cancer Research Center–Center for Molecular Biology Alliance, Heidelberg, Germany
[2]Nikon Imaging Center at the University of Heidelberg, Bioquant, Heidelberg, Germany

The spindle pole body (SPB) of budding yeast duplicates once per cell cycle. In G1, the satellite, an SPB precursor, assembles next to the mother SPB (mSPB) on the cytoplasmic side of the nuclear envelope (NE). How the growing satellite subsequently inserts into the NE is an open question. To address this, we have uncoupled satellite growth from NE insertion. We show that the bridge structure that separates the mSPB from the satellite is a distance holder that prevents deleterious fusion of both structures. Binding of the γ-tubulin receptor Spc110 to the central plaque from within the nucleus is important for NE insertion of the new SPB. Moreover, we provide evidence that a nuclear pore complex associates with the duplicating SPB and helps to insert the SPB into the NE. After SPB insertion, membrane-associated proteins including the conserved Ndc1 encircle the SPB and retain it within the NE. Thus, uncoupling SPB growth from NE insertion unmasks functions of the duplication machinery.

Introduction

The spindle pole body (SPB) provides microtubule (MT) organizing functions in fungi. The SPB of *Saccharomyces cerevisiae* is a multilayered structure that is embedded in the nuclear envelope (NE) throughout the cell cycle (Jaspersen and Winey, 2004). EM studies identified several SPB substructures. The central plaque is the SPB substructure that interacts with the fusion site of the inner and outer NE (Byers and Goetsch, 1975). The bridge is an extension of the central SPB and is layered on top of the cytoplasmic and nuclear sides of the NE. In early G1, the satellite, a miniature version of the SPB, assembles on the distal end of the cytoplasmic side of the bridge (Byers and Goetsch, 1975; Adams and Kilmartin, 1999). Once cells have passed the start of the cell cycle, the satellite grows in size into a duplication plaque (DP) that inserts simultaneously with its growth into the NE (Adams and Kilmartin, 1999).

SPB components important for SPB duplication and NE insertion have been identified through genetic screens and proteomic approaches (Rout and Kilmartin, 1990; Kilmartin, 2003; Jaspersen and Winey, 2004). The protein Sfi1 is a conserved, elongated half bridge and bridge component on the cytoplasmic side of the NE (Kilmartin, 2003; Li et al., 2006; Burns et al., 2015; Seybold et al., 2015). The satellite assembles on the distal end of the bridge that contains Sfi1 N termini (Kilmartin, 2003, 2014). The composition of the satellite reflects the composition of the cytoplasmic side of the SPB as Spc42, Spc29, Cnm67, and Nud1 are well-characterized satellite components (Donaldson and Kilmartin, 1996; Elliott et al., 1999; Gruneberg et al., 2000; Schaerer et al., 2001; Burns et al., 2015).

Several SPB components, Bbp1, Mps2, Nbp1, and Ndc1, are important for the insertion of the new SPB into the NE. These interacting proteins have been collectively named the SPB insertion network (SPIN; Rüthnick and Schiebel, 2016). Inactivation of SPIN genes through conditional lethal mutations generates a dead pole that sits on the cytoplasmic side of the NE (Winey et al., 1991; Araki et al., 2006). This indicates that SPIN components are involved in insertion of the new SPB into the NE, although the molecular function is unclear.

Genetic data suggest a functional interplay between SPIN and nuclear pore complex (NPC) components. Although normally essential for viability, *MPS2* and *MPS3* can be deleted if cells lack in addition the nuclear pore membrane genes *POM152*, *POM34*, or *MLP1/2* (Sezen et al., 2009; Witkin et al., 2010). Also, an enrichment of NPCs at the vicinity of SPBs that has been detected by EM analysis (Winey et al., 1997) and high-resolution microscopy (Wang et al., 2016) suggests that NPCs may play a more direct role in SPB NE insertion.

In this study, we have uncoupled growth of the new SPB from NE insertion. This enabled us to identify several steps of the SPB duplication pathway. First, the satellite is elongated and angled relative to the NE. Second, the Spc42 polymer is

fusogenic; experimental data suggest that one function of the bridge is to separate the Spc42 layers of the mother SPBs (mSPBs) and daughter SPBs (dSPBs). Third, Spc42 layers attach and probably mix partially during karyogamy when SPBs fuse. Fourth, Spc110 recruitment to the DP is required for proper SPB insertion into the NE. Fifth, the inserted SPB is surrounded by a ring of SPIN proteins that anchor the SPB within the NE. Finally, we show that the duplicating SPB recruits NPCs to the insertion site. Analysis of cells with impaired NPCs indicate that NPCs play an important role in SPB insertion.

Results

Upright orientation of the satellite

NE deformation by the assembling NPC that leads to NE fusion was recently reported in human cells (Otsuka et al., 2016). This raises the possibility that a similar deformation step early in SPB duplication promotes its insertion into the NE. An earlier EM study indicated that the growing DP is angled relative to the mSPB and might push the two leaflets of the NE together (Adams and Kilmartin, 1999). To determine whether DP growth has a mechanistic impact on the insertion of the new SPB into the NE, we unlinked both events. Overexpression (OE) of *SPC42* expands the central plaque of the SPB by radial elongation of the 2D Spc42 crystal (Donaldson and Kilmartin, 1996; Bullitt et al., 1997). Because Spc42 is also a component of the satellite (Adams and Kilmartin, 1999), we tested whether *SPC42* OE in α-factor–arrested cells would expand the Spc42 layer in the satellite as well. Besides single *SPC42* OE, we combined the *SPC42* OE with its interaction partner *SPC29* to determine whether this regimen would have an impact on satellite expansion. We reasoned that, if *SPC42* OE triggers expansion of the satellite, α-factor washout would allow us to study the insertion of this polymer into the NE independently of DP growth.

Addition of galactose to α-factor–arrested cells activated the pGal1 promoter and resulted in a rapid accumulation of Spc42 but also of Spc29, possibly reflecting stabilization (Figs. 1 and S1 A). Similarly, both proteins rapidly accumulated in α-factor–arrested cells cooverexpressing *SPC42* and *SPC29* (*SPC42 SPC29* OE; Fig. S1 A). We used these strains to determine how the SPB of α-factor–arrested cells responded to *SPC42 SPC29* OE by structured illumination microscopy (SIM). The γ-TuSC receptor Spc110–yeast-enhanced GFP (yeGFP) was used as a marker for the mSPB. At 0 min, cells showed two adjacent Spc42-mCherry signals. Only the stronger of the two signals associated with Spc110-yeGFP, indicating that it was the mSPB (Fig. 1 B). We measured the full width at half maximum (FWHM) of the mSPB (Fig. 1 B, white dashed lines) and satellite (Fig. 1 B, yellow dashed lines) via plot profiles in *SPC42 SPC29* OE cells (Fig. 1 C). This analysis revealed a nearly linear increase in satellite size over the duration of the OE period, whereas the mSPB signal remained relatively constant (Fig. 1, C and D). This suggests preferential incorporation of Spc42 into the satellite in G1 cells.

Strikingly, EM analysis of G1-arrested cells expressing *SPC42* or *SPC42 SPC29* identified an obelisk-like structure at the distal end of the bridge in ∼60% of the cells (Fig. 1 E). Quantification experiments, SIM, and immuno-EM suggest that this polymer contained Spc42 and Spc29 (Fig. S1, B–D). Surprisingly, the obelisk was orientated such that it stood upright relative to the NE (Fig. 1 E). *SPC42 SPC29* OE gave similar results as expression of *SPC42* alone. However, the obelisk was nearly three times longer when both genes were simultaneously expressed (Fig. 1 E). In contrast to cycling cells (Bullitt et al., 1997) and consistent with our SIM data (Fig. 1 D), the Spc42 layer in the mSPB was only slightly enlarged by *SPC42* or *SPC42 SPC29* OE. Thus, in G1 cells, the Spc42 layers in the mSPB and the satellite have different orientations and polymerization properties.

To strengthen the notion that the Spc42 layer in the satellite is angled relative to the NE, we analyzed the morphology of the satellite in WT cells by thin-section EM. The EM micrographs showed that the satellite was not spherical but rather had the appearance of an elongated structure. The length axis of the satellite was not parallel but was orientated at an angle relative to the NE. The satellite was connected to the bridge on its NE-directed side (Fig. 1 F, left). The appearance of the satellite was identical in α-factor–arrested pGal1-*SPC42* pGal1-*SPC29* cells grown in the absence of galactose (Fig. 1 F, right). A very similar satellite structure was observed in cells arrested in G1 by the depletion of the G1 cyclins *CLN1–CLN3* (Fig. S1 E; Jeoung et al., 1998), indicating that the satellite morphology was not changed by α-factor incubation. Thus, the satellite is an elongated structure that resides with an orientation that is at an angle relative to the NE.

### The Spc42 layer has fusogenic properties

We next analyzed the fate of the Spc42–Spc29 obelisk by EM. Interestingly, 30 min after α-factor washout, the obelisk was either lying on top of the NE on the opposite side to the bridge and the mSPB or had flipped toward the mSPB (Fig. 2 A). The latter went hand in hand with the fusion of the obelisk and the mSPB into one continuous layer that arched the bridge (Fig. 2 A, right). Intriguingly, in both cases, the Spc42–Spc29 obelisk remained connected to the distal end of the bridge. Immuno-EM analysis revealed Mps2 near the point at which the arched Spc42–Spc29 structure was anchored (Fig. S2 A), raising the possibility that Mps2 constitutes part of the NE anchor.

To rule out the possibility that the fusogenic property of the Spc42 layer is a consequence of the G1 arrest, cells were treated for 1 h with the MT depolymerizer nocodazole. This treatment arrested cells with side-by-side SPBs in mitosis (Fig. S2 B, left; Jacobs et al., 1988). Next, *SPC42 SPC29* were overexpressed in the presence of nocodazole. EM analysis showed the fusion of the two SPBs into one layer (Fig. S2 B, right). In >90% of control cells without pGal1 induction, nocodazole washout promoted SPB separation (Fig. S2 C). In contrast, in cells with *SPC42 SPC29* OE, nocodazole washout did not allow SPB separation, consistent with fusion of the two SPBs.

This unexpected fusogenic property of the Spc42 polymer provides an explanation for the need to separate the mSPB from the satellite during the duplication process. The presence of a bridge structure that separates the mSPB from the satellite by a distance of ∼120 nm ensures that expansion of the satellite generates the separate entity of the dSPB rather than creating a fusion with the existing mSPB. The length of the bridge is determined by bundles of antiparallel Sfi1 molecules that intersect in the bridge center (Kilmartin, 2003; Li et al., 2006; Seybold et al., 2015). To test this hypothesis of the bridge acting as an insulator, we constructed bonsai versions of Sfi1. Surprisingly, most of the *SFI1* mutants did not support cell growth, most likely because deletions of the central centrin-binding repeats affected the structure or orientation of Sfi1. However, we
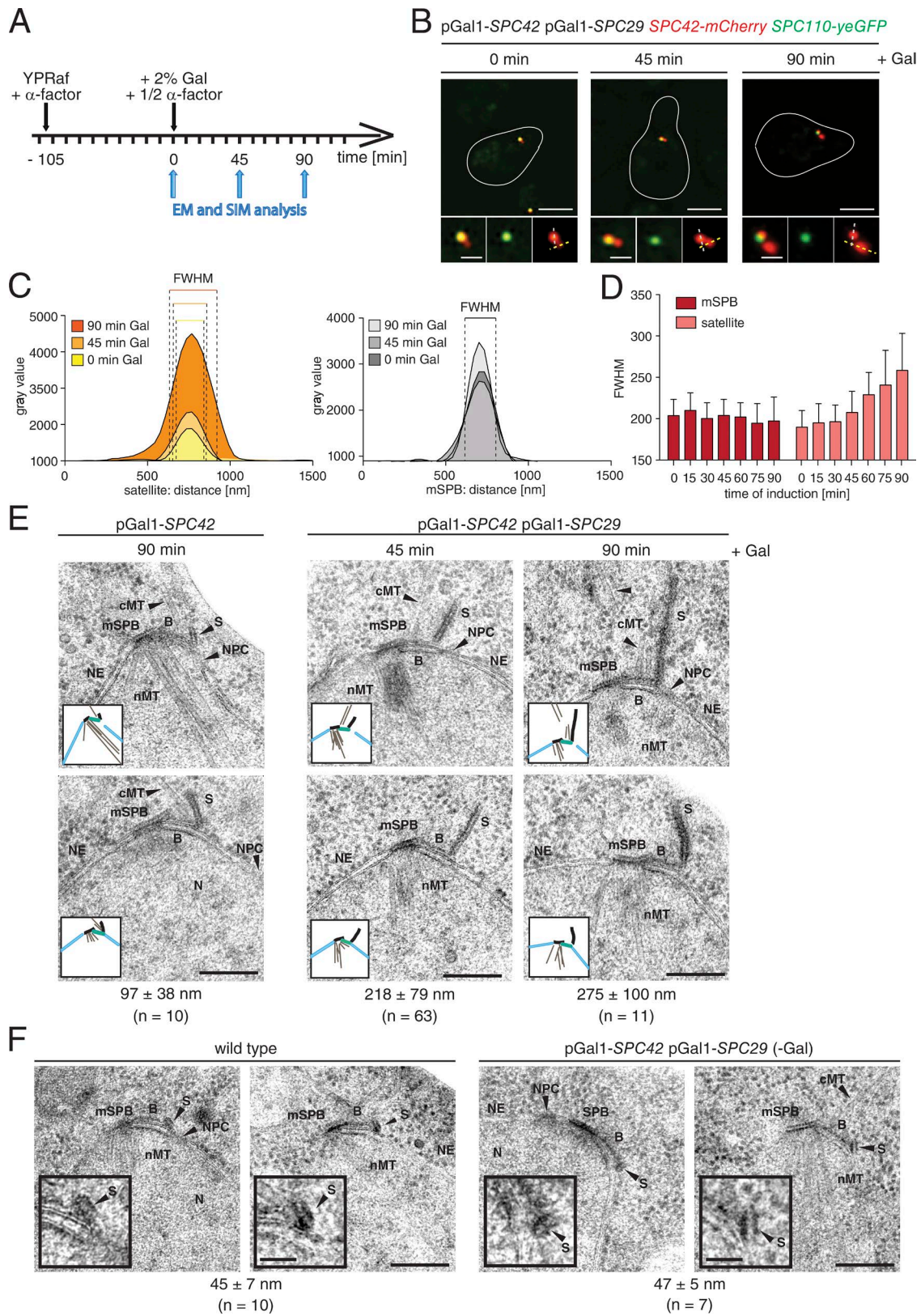
Figure 1. **The upright orientation of the satellite.** (A) Experimental outline. (B) SIM analysis in α-factor–arrested and *SPC42 SPC29* OE–induced (+Gal) cells. White (mSPB) and yellow (satellite) dashed lines indicate the plot profile measurements in C. Bars: (main images) 2 µm; (insets) 500 nm. (C) Exemplary FWHM quantification of the plot profiles from B. (D) FWHM quantifications of B. Error bars indicate SD. $n \geq 30$. (E) EM analysis of α-factor–arrested cells upon *SPC42* or *SPC42 SPC29* OE. Cartoons illustrate SPB phenotypes. (F) Representative EM images of WT cells and noninduced pGal1-*SPC42* pGal1-*SPC29* cells arrested in α-factor. (E and F) The length of the obelisk and satellite was quantified. Numbers of cells ± SD. Bars: (main images) 200 nm; (insets) 50 nm. B, bridge; cMT, cytoplasmic MT; N, nucleus; nMT, nuclear MT; S, satellite.
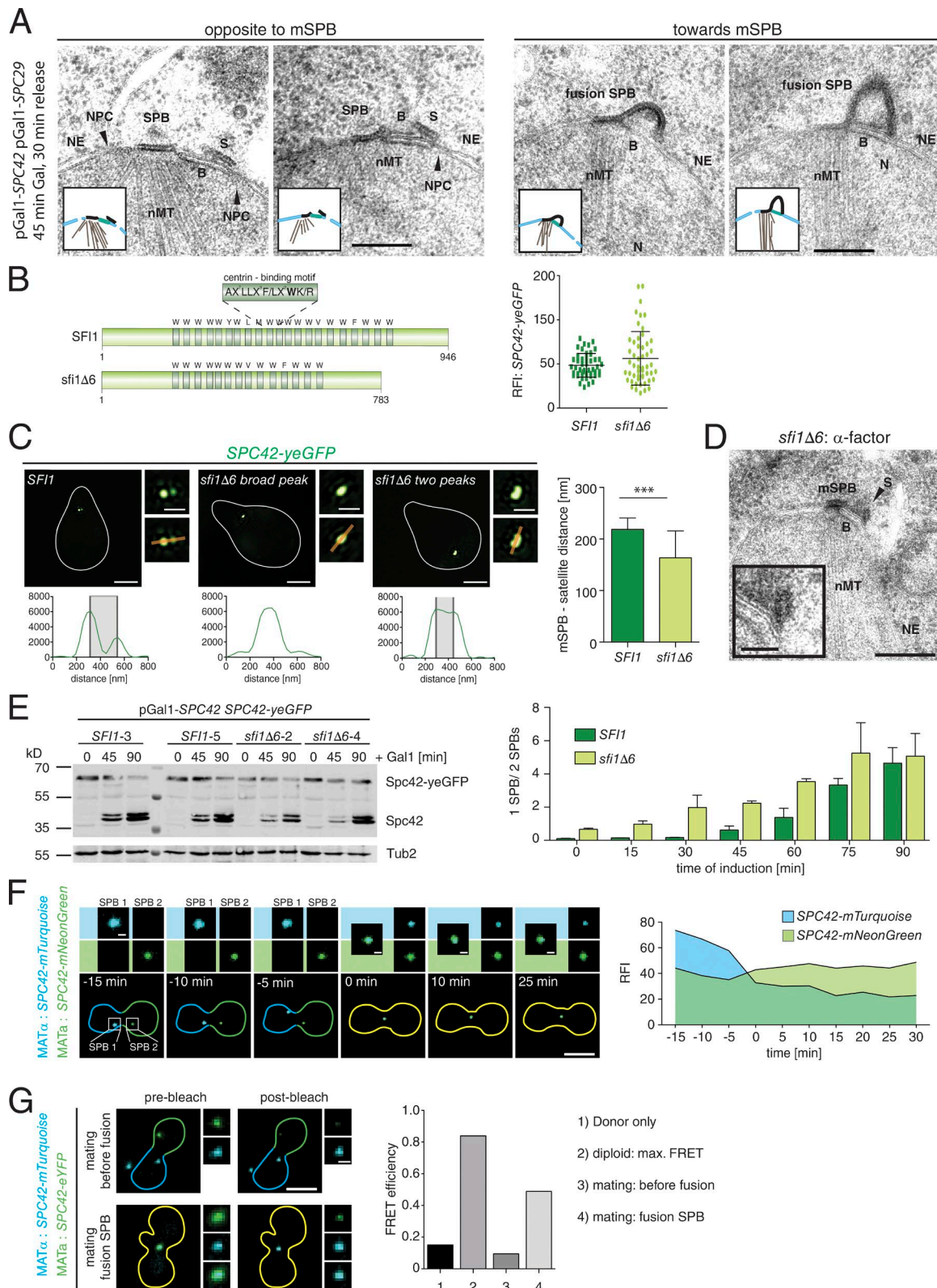
Figure 2. **The bridge serves as an insulator.** (A) EM micrographs of cells (45 min *SPC42 SPC29* OE in α-factor and then 30 min release). Cartoons illustrate SPB phenotypes. Bars, 200 nm. (B) Schematic view of Sfi1 WT and sfi1Δ6 proteins. Cells were arrested in α-factor for Spc42-yeGFP intensity measurement. n ≥ 50. (C) Exemplary SIM images of *SFI1* and *sfi1Δ6* cells arrested in α-factor. Orange lines indicate how the plot profiles were generated. Gray lines in the plot profiles show the distance between two peaks. Quantification of the mSPB satellite distance. *SFI1*: n = 52; *sfi1Δ6*: n = 9. Error bars indicate SD. ***, P < 0.0001. Bars: (main images) 2 µm; (insets) 500 nm. (D) EM micrograph of an α-factor–arrested *sfi1Δ6* cell. Bars: (main images) 200 nm; (insets) 50 nm. (E) Western blot verification of Spc42 OE and quantification of phenotypes from live-cell imaging. Mean of two experiments with >200 cells analyzed for each experiment per time point. Error bars indicate SD. (F) Live-cell imaging of MATα *SPC42-mTurquoise* cells mating with MATa

obtained one viable deletion in *SFI1* (*sfi1Δ6*; Fig. 2 B, left). *sfi1Δ6* cells formed a satellite in α-factor–arrested cells, as indicated by SPC42-yeGFP fluorescence quantification (Fig. 2 B, right). The distance between the mSPB and the satellite was reduced from 220 nm in WT to 160 nm in the *sfi1Δ6* mutant cells as determined by SIM measurements from peak-to-peak intensity (Fig. 2 C). Notably, most of the *sfi1Δ6* mSPB-satellite pairs could not be resolved into two distinct signals, reflecting the diminished separation of the partners. EM confirmed this shortened bridge phenotype from 120 nm in WT (Li et al., 2006) to 78 nm in the *sfi1Δ6* cells (Fig. 2 D).

With this mutant in hand, we tested the function of the bridge as an insulator. The idea behind this experiment was that fusion between the Spc42 obelisk and the mSPB is dependent on the length of both the bridge and the obelisk. We arrested *SFI1* and *sfi1Δ6* cells with satellite-bearing SPBs in G1 followed by galactose-induced expression of *SPC42* from 0–90 min. Expression of *SPC42* was similar in *SFI1* and *sfi1Δ6* cells (Fig. 2 E, left). Cells were released into the cell cycle in the presence of the suppressing glucose, and the SPB phenotype of large-budded cells was analyzed over time. We calculated the ratio of cells with one SPB versus two SPBs. A value close to 0 indicated that most cells had two SPBs. In *SFI1* cells, a critical value was *t* = 60 min when more than half the cells showed one fused SPB after α-factor washout (SPB ratio >1). Importantly, *sfi1Δ6* cells had already reached this threshold after 15–30 min (Fig. 2 E, right). This experiment strongly suggests that one of the functions of the bridge is to separate the fusogenic Spc42 layers of the satellite and mSPB in G1/S phase of the cell cycle.

Spc42 layer fusion during karyogamy

The question of the relevance of the fusion event between the mSPB and the obelisk drew our attention to yeast mating. During mating, the cell bodies of MATα and MATa cells fuse, and this is followed by karyogamy (Kurihara et al., 1994). One of the steps in karyogamy is the fusion of the two SPBs (Byers, 1981a; Melloy et al., 2007). To analyze this process in greater detail, we performed fluorescence resonance energy transfer (FRET) experiments during mating of MATα *SPC42-mNeonGreen* and MATa *SPC42-mTurquoise* cells. Live-cell image analysis showed a clear reduction in the FRET donor signal and a slight increase in the accepter fluorescence intensity with the SPB fusion event (Fig. 2 F; *t* = 0). This indicates at least partial fusion of the two SPB Spc42 layers.

To confirm this result, we performed accepter photobleaching with the FRET pair mTurquoise as donor and enhanced YFP (eYFP) as accepter fluorophore. Cells expressing only *SPC42-mTurquoise* served as negative donor controls. Maximum FRET efficiency was measured in diploid *SPC42-eYFP/SPC42-mTurquoise* cells in which the SPB comprised a layer throughout which Spc42-eYFP and Spc42-mTurquoise were evenly distributed. Next, we performed accepter photobleaching at different stages of the mating process. No FRET signal was measured before karyogamy. However, a FRET signal appeared at the SPB upon fusion of the two SPBs (Fig. 2 G). To test for the exchange of Spc42 molecules from

both cell pools, nocodazole was added to mating Spc42-eYFP and Spc42-mTurquoise cells to prevent karyogamy/SPB fusion, which usually take place within 15 min after cell fusion (Gibeaux et al., 2013). The appearance of Spc42-eYFP in the Spc42-mTurquoise SPB was quantified to analyze the exchange between both Spc42 pools. The result indicates that there was only minor recruitment of Spc42-eYFP to the Spc42-mTurquoise SPB 30 min after nocodazole addition (Fig. S2 D, mating: before SPB fusion and right images). These data are suggestive of binding and partial mixing of the Spc42-eYFP and Spc42-mTurquoise layers of the two SPBs during SPB fusion as part of the mating process.

Insertion of the Spc42–Spc29 polymer into the NE

The satellite-derived Spc42–Spc29 obelisk fused with the mSPB shortly after α-factor removal or became layered onto the cytoplasmic surface of the NE opposite to the mSPB (Fig. 2 A). In the latter case, cells separated the two SPBs and assembled a mitotic spindle as determined by live-cell imaging (Fig. 3 A). Analysis of this class by EM showed two NE-inserted SPBs (Fig. 3 B). Live-cell imaging also showed arrested large-budded cells with a single SPB (Fig. 3 C). This phenotype most likely reflects the product of an SPB fusion event. In this study, the arched Spc42 polymer (Fig. 2 A) flattened on top of the NE (Fig. 3 D). It either resided on top of the bridge while still being anchored to its distal end (class I), or it detached from the bridge end and now covered the nuclear rim where the DP normally inserts (class II). In class I, the mSPB was >200 nm and therefore larger than the SPBs of WT cells. Moreover, the central plaque of the mSPB frequently detached from the NE. Collectively, these data suggest that the Spc42–Spc29 fusion structure had inserted into the opening of the mSPB. In the second class, the Spc42–Spc29 portion that occupied the nuclear rim on the opposite side of the bridge to the mSPB eventually organized nuclear MTs, indicative of insertion into the NE, while remaining connected to the mSPB (Fig. 3 D). This most likely reflects the normal insertion of the DP.

At later time points, the fusion SPB was completely embedded in the NE in all cells. The enlarged SPBs organized two directional MT bundles, suggestive of two distinct functional domains (Fig. 3 E). Consistent with this notion, fused SPBs showed two pronounced central-plaque Spc42-mCherry densities by SIM (Fig. 3 F). These findings suggest that cells can insert the fused SPB into the NE via either the opening provided by the mSPB or into an opening at the distal end of the bridge.

SPIN components at the inserting SPB

To gain insight into the function of SPIN proteins beyond NE fusion, we followed the signal intensity of yeGFP-tagged SPIN proteins by live-cell imaging. This was done in WT cells and cells with a G1-assembled Spc42–Spc29 obelisk. First, we analyzed Spc110-yeGFP in WT because Spc110 recruitment to the SPB marks the time point at which the new SPB inserts into the NE (Kilmartin et al., 1993; Elliott et al., 1999). Spc110-yeGFP was recruited between 20 and 32 min after α-factor release, and the signal decreased, with SPB separation between 32 and

---

SPC42-mNeonGreen cells. Representative cells are shown together with signal intensity quantification. (G) Accepter photobleaching at different stages of mating. FRET efficiency was calculated. Bars: (main images) 5 μm; (insets) 500 nm. B, bridge; cMT, cytoplasmic MT; N, nucleus; nMT, nuclear MT; RFI, relative fluorescence intensity; S, satellite.
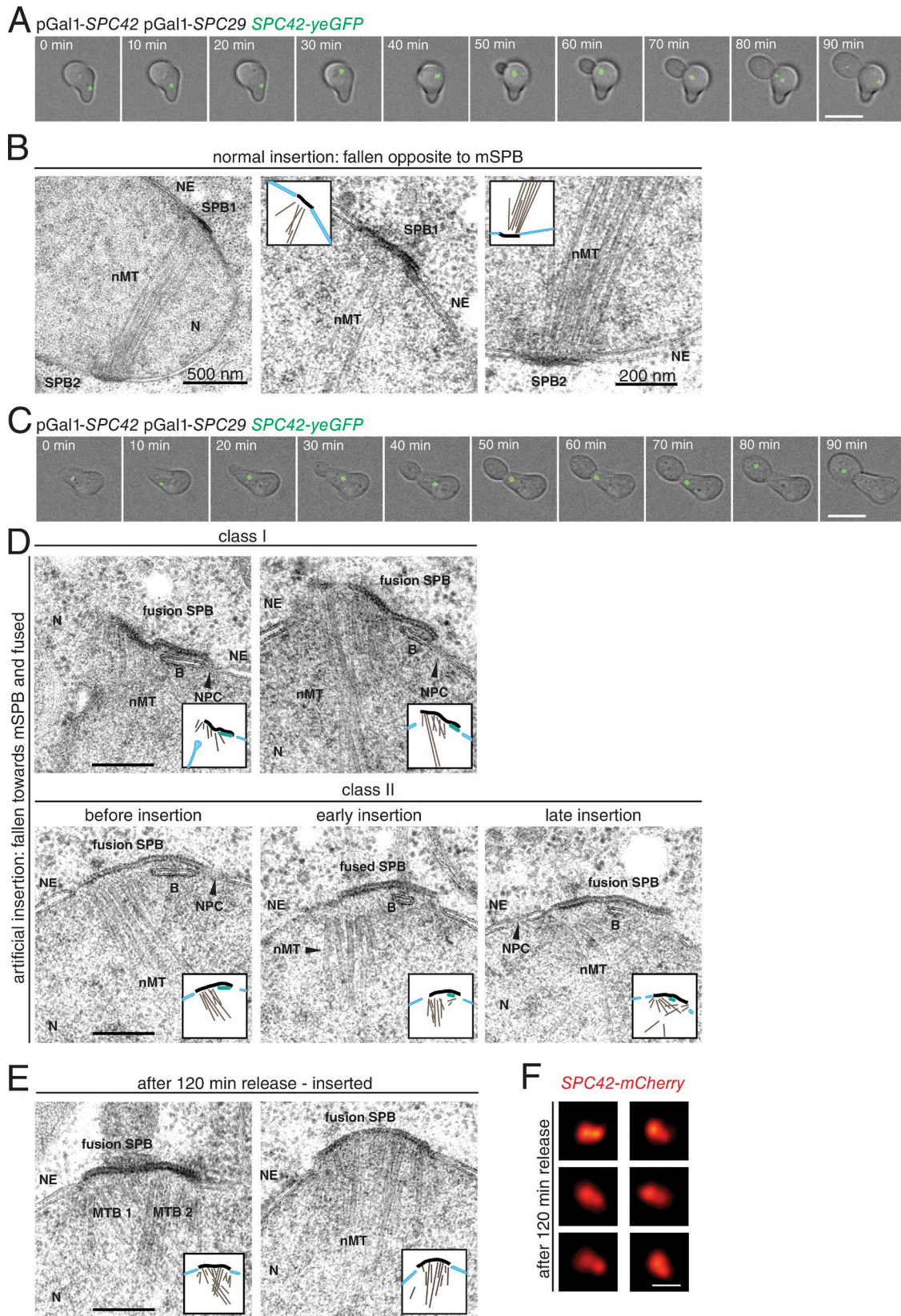
Figure 3. **Insertion phenotypes.** (A–F) Cells arrested with α-factor followed by *SPC42 SPC29* OE for 45 min before release into cell cycle. (A and C) Live-cell imaging for 90 min after release. (B, D, and E) EM was conducted after 30-min (B and D) or 120-min release (E). Cartoons illustrate the state of the SPB. (F) Representative SIM images of *SPC42-mCherry* in *SPC42 SPC29* OE cells after 120 min release. Bars: (A and C) 4 μm; (D and E) 200 nm; (F) 500 nm. B, bridge; N, nucleus; nMT, nuclear MT; S, satellite.

36 min (Fig. 4 A, unicolor and stripped areas). In contrast, the bridge component Sfi1-yeGFP that has already incorporated into the duplicating SPB before α-factor arrest (Burns et al., 2015; Seybold et al., 2015) remained constant between 0 and 32 min and then split in half with SPB separation. All SPIN components including Mps3 showed an increase in signal intensity with SPB insertion followed by a drop during SPB separation (Fig. 4 A). Thus, SPIN proteins are recruited during the insertion of the SPB into the NE.

We next followed all proteins during NE insertion of the Spc42–Spc29 obelisk in *SPC42 SPC29* OE cells. We analyzed fused SPBs as indicated by the absence of SPB separation 60 min after α-factor release. Between 20 and 40 min, the Spc42–Spc29 layer inserted into the NE as indicated by the increase in Spc110-yeGFP signal (Fig. 4 A, scatter plots). Interestingly, ~50% more Spc110-yeGFP was recruited to fused SPBs than to WT SPBs, probably as a reflection of the increased size of the fusion SPB (Fig. 4 A; black line reflects maximum signal in WT cells). Consistent with a function as bridge component and the lack of SPB separation, Sfi1-yeGFP signal intensity remained constant over time. Ndc1-yeGFP, yeGFP-Mps2, and Bbp1-yeGFP were all recruited with higher signal intensity to the fused SPB than to the duplicated WT SPB. This signal enhancement suggests that these SPIN components probably interact with the large Spc42–Spc29 layer during NE insertion. In contrast, the signals from Nbp1-yeGFP and yeGFP-Mps3 did not change in response to the increased size of the fusion SPB (Fig. 4 A).

We studied the localization of SPB components by SIM. Considering the large size of the fused SPB (>200 nm), this approach had the potential to detect structures that are difficult to resolve in WT cells. As reported previously (Burns et al., 2015), in α-factor WT cells, yeGFP-Mps2 and Bbp1-yeGFP associated with the mSPB and the satellite. In contrast, Ndc1-yeGFP and Nbp1-yeGFP associated predominately with the mSPB (Fig. S3, A and B). *SPC42 SPC29* OE in α-factor cells did not change these localization patterns, with the exception of Bbp1-yeGFP—for unknown reasons, Bbp1-yeGFP was now mainly associated with the mSPB (Figs. 4 B and S3, A and B). However, combined OE of *BBP1* along with *SPC42 SPC29* restored the dual localization of Bbp1, which indicates that upon *SPC42 SPC29* OE, Bbp1 distribution is governed by the limitation of a finite quantity of Bbp1 (Fig. S3 C).

Analysis of the SPB fusions 120 min after α-factor washout revealed two intense foci of Spc42-mCherry (Fig. 3 F). Interestingly, a view of the fused SPB from above revealed a ring of Ndc1-yeGFP, yeGFP-Mps2, Bbp1-yeGFP, and Nbp1-yeGFP that encircled the large embedded fusion SPB. Such rings were not observed in α-factor–arrested cells (Figs. 4 B and S3 A) or 30 min after α-factor washout when the Spc42–Spc29 fusion just started to insert into the NE (Fig. S3 A). Thus, Ndc1, Mps2, Bbp1, and Nbp1 probably encircle the NE-inserted SPB but do not form a pore before insertion. In contrast, Mps3 and Sfi1 foci were detected in between the twin Spc42 signals or were enriched more toward one site (Fig. 4 B). These localizations likely reflect cells where the Spc42–Spc29 layer overlaid the bridge and inserted adjacent to the bridge, or at the mSPB into the NE, respectively (Fig. 3 D). Collectively, these data indicate that Ndc1, Nbp1, and the Bbp1–Mps2 complex encircle the inserted SPB core.
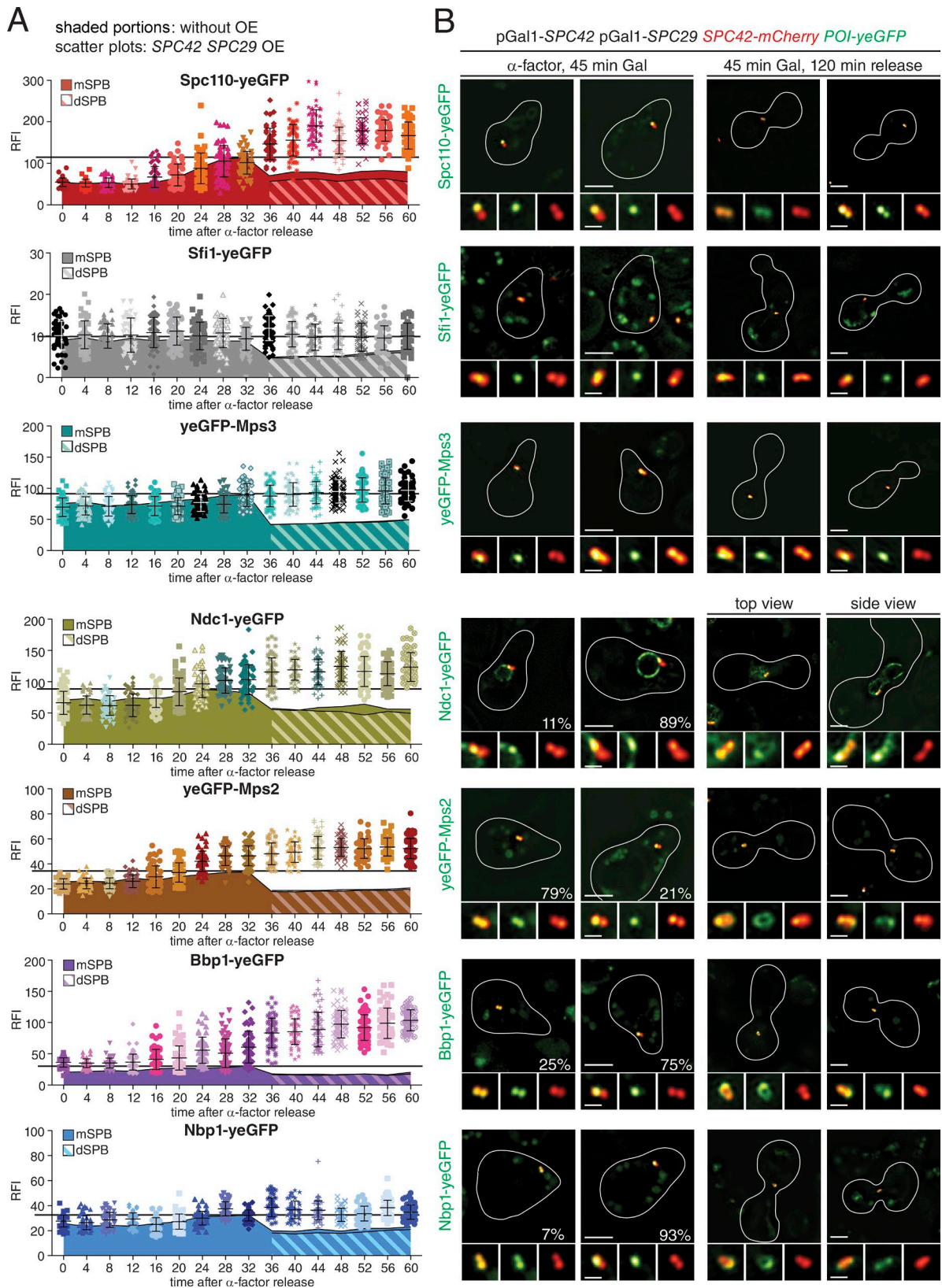
Conditional lethal *spc110* mutant cells affect NE insertion of the dSPB

Analysis of conditional lethal SPB duplication mutants in combination with *SPC42 SPC29* OE may reveal novel functions of SPB components. We first compared the impact of *SPC42 SPC29* OE in *spc110(ts)* mutant and *SPC110* WT control cells. We used *SPC110* mutants that were defective in either calmodulin or Spc29 binding but retained the ability to interact with the γ-tubulin complex (Fig. S4 A; Kilmartin and Goh, 1996; Stirling et al., 1996; Elliott et al., 1999). To ensure that the mutated Spc110 proteins showed reduced binding to SPBs, we followed Tub4-yeGFP signal intensity at Spc42-mCherry–marked SPBs as outlined in Fig. 5 A. Only fused SPBs were analyzed.

In *SPC110* WT cells with *SPC42 SPC29* OE, the Tub4-yeGFP signal strongly increased with the insertion of the Spc42–Spc29 layer into the NE 20 min after α-factor washout because of the recruitment of Tub4 to the SPB (Fig. 5 B, shaded portion). Consistently, these SPBs nucleated a dense layer of MTs (Fig. 5 C). In contrast, SPBs of *spc110-124*, *spc110-2*, and *spc110-120* cells contained little Tub4-yeGFP even at the time of NE insertion of the fusion SPB (Figs. 5 B and S4 B, scatter plots), confirming that Spc110 was nonfunctional in these cells. EM analysis showed that the fusion SPB of synchronized *spc110-124* cells was similar in size as in WT *SPC110* cells. However, in *spc110-124* cells, the SPB resided on top of the cytoplasmic side of the NE and organized only a small number of nuclear MTs through several openings within the NE (Fig. 5 D). The disturbed NE insertion of the fusion SPB in *spc110-124* cells suggests that binding of Spc110 to the Spc42–Spc29 interface is important for the proper insertion of the new SPB into the NE.

SPIN components anchor the fusion SPB in the NE

Because the SPB of *SPC42 SPC29* OE cells can insert into the opening of the mSPB without NE fusion, SPIN mutants in combination with *SPC42 SPC29* OE may indicate functions that are otherwise masked by the "dead pole" phenotype. We applied the experimental regimen of Fig. 5 A to the analysis of the impact of conditional lethal *ndc1*, *mps2*, *bbp1*, and *nbp1* mutations upon the insertion process. EM analysis of *ndc1-39* cells revealed fused SPBs that had partially lost their attachment to the NE (Fig. 5 E). Interestingly, *mps2-42*, *bbp1-1*, and *nbp1-2* (Fig. S4 C) cells revealed an even more drastic phenotype in which the SPB detached completely from the NE (Fig. 5 E) and were situated in either the nucleus or the cytoplasm. These phenotypes are consistent with an NE anchoring function for Ndc1, Bbp1, Mps2, and Nbp1. Furthermore, all SPIN mutants displayed the expected dead pole phenotype in which the mSPB was inserted into the NE, whereas the dSPB failed to insert into the NE and therefore did not carry any nuclear Spc110 (Fig. S4 D, [left] and E [top]). Finally, we observed cells with a "lost SPB," in which one dead SPB carrying a Spc42-mCherry signal alone, without an accompanying Spc110-yeGFP signal, was distinct from a single focus of Spc110-yeGFP that was not marked by Spc42-mCherry. In the EM analysis, we observed a disintegration of SPBs that correlated with a corresponding fluorescence microscopy phenotype (Fig. S4 D [right] and E [bottom]). We conclude that the Bbp1–Mps2 complex, Nbp1, and Ndc1 have functions associated with the anchorage of the SPB in the NE.

Figure 4. **Localization of the SPIN components upon NE insertion of the Spc42–Spc29 obelisk.** (A) Fluorescence intensity quantification of the yeGFP signal of indicated proteins at the SPB after release from the G1 block in WT cells (shaded portions in graphs) and cells upon 45 min *SPC42 SPC29* OE (scatter plot). Error bars indicate SD; $n \geq 50$. The black horizontal line indicates the maximum yeGFP intensity at the duplicated SPB without *SPC42 SPC29* OE. RFI, relative fluorescence intensity. (B) SIM images of *SPC42 SPC29* OE cells in α-factor arrest and after 120 min release. Bars: (main images) 2 µm; (insets) 500 nm.
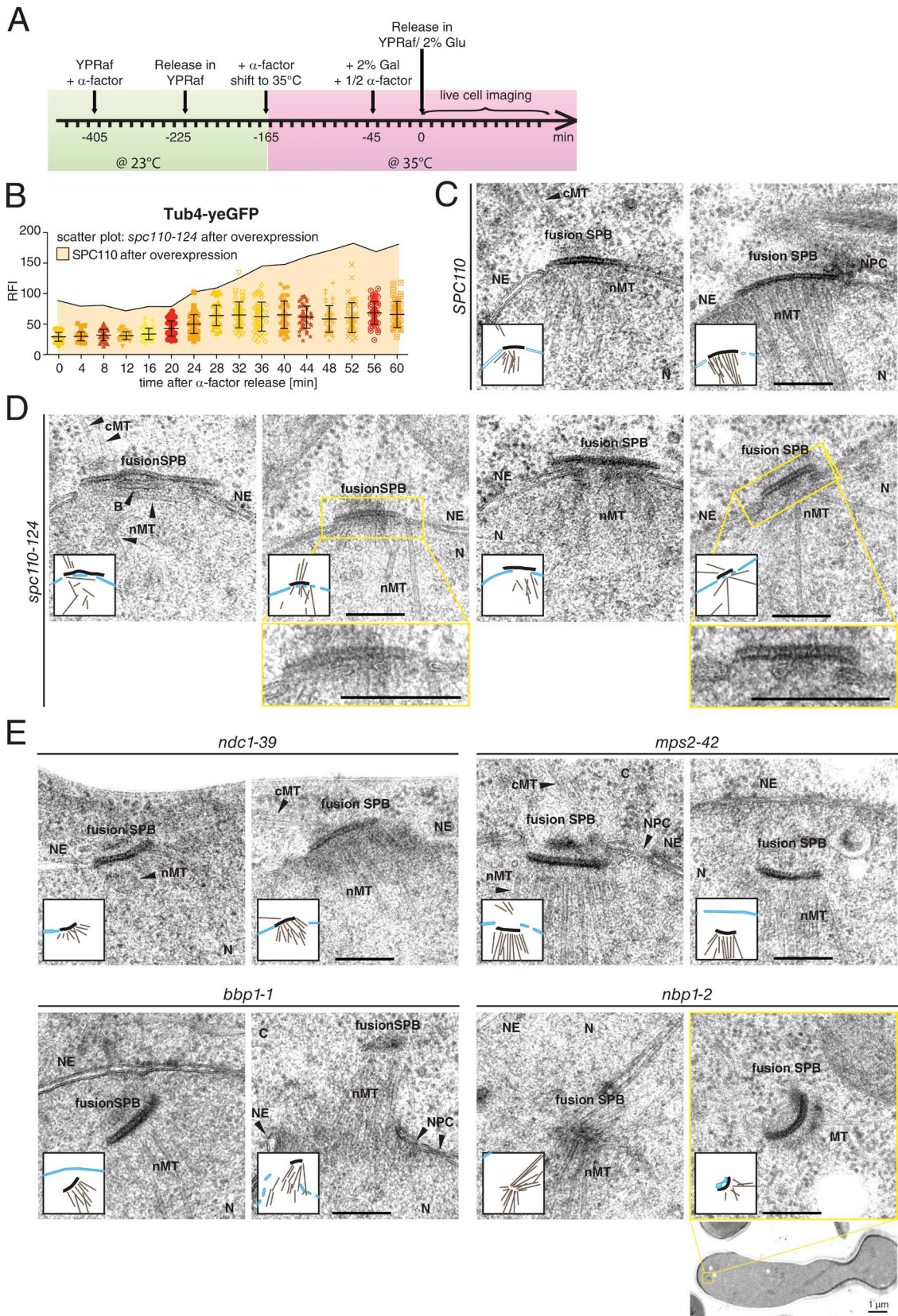
Figure 5. **Analysis of SPB duplication mutants.** (A) Experimental outline. (B) Fluorescence intensity quantification for Tub4-yeGFP in *spc110-124* mutant cells (scatter plot) in comparison to *SPC110* WT (shaded portion in graph) upon 45 min *SPC42 SPC29* OE. Error bars indicate SD. $n \geq 50$. (C and D) Representative EM micrographs of *SPC110* WT (C) and *spc110-124* (D) cells 60 min after cell cycle release from α-factor arrest and *SPC42 SPC29* OE. (E) EM micrographs of SPIN ts mutant cells after G1 block, *SPC42 SPC29* OE, and 60 min release. (C–E) Cartoons illustrate SPB phenotypes. Bars, 200 nm. B, bridge; cMT, cytoplasmic MT; N, nucleus; nMT, nuclear MT; RFI, relative fluorescence intensity.

Recruitment of an NPC to the SPB insertion site

A pore in the NE that is indistinguishable from NPCs was seen next to the DP (Adams and Kilmartin, 1999). We considered the possibility that this pore may, in some way, assist SPB duplication. We therefore asked whether NPCs are associated with the duplicating SPB. To reduce the NPC density, we exploited mutations that cause NPCs to cluster in one area of the NE (Wente and Blobel, 1994). Cluster mutant cells displayed a weak NPC signal close to the SPBs, as indicated by the colocalization of Nic96-yeGFP and Spc42-mCherry (Fig. 6 A), whereas the majority of the NPC signal resided within other domains of the NE. However, this was a dynamic event because live-cell imaging revealed that the Nic96-yeGFP signal moved back and forth from the SPB (Fig. 6 B, yellow arrows). The association of the NPC signal with the SPB persisted even when the SPB moved into the daughter cell in anaphase (Fig. 6, A and B). This colocalization was also observed for the NPC components Mlp1, Mlp2, Nup159, Nup170, and Nup145 (Fig. 6 C). In contrast, the NPC component Nup2, which is released from the NPC into the nucleus in the cluster mutants (Denning et al., 2001), showed no specific interaction with the SPB. Thus, NPCs are able to associate with SPBs.

We next monitored the localization of NPCs in cells with *SPC42 SPC29* OE because this overproduction enabled us to identify SPB substructures with ease. SPBs of α-factor–arrested and –released cells were frequently associated with an opening of the NE close to the Spc42–Spc29 layer (Figs. 1, 2, and 3). Immuno-EM with an antibody against the NPC component Nsp1 (Grandi et al., 1995) confirmed that this structure constituted an NPC (Fig. 7 A). Furthermore, the NPC was also confirmed by α-Nsp1 immuno-EM in α-factor–arrested WT cells (Fig. 6 D) and G1-arrested *Δcln1 Δcln2* pGal1-*CLN3* cells (Fig. 6 E). To understand whether NPCs specifically associate with the duplicating SPB, we reanalyzed EM images (tilted and serial sections) according to their SPB morphology, as summarized in Fig. 7 B. This analysis revealed a gradual transition in SPB phenotypes from the upright satellite (string SPB) to the formation of a fusion SPB through the stage of partial NE insertion of the fusion SPB to the point of full SPB insertion in *SPC42 SPC29* OE cells. SPB phenotypes were then correlated with NPC abundance. NPC occupancy at the distal end of the bridge of α-factor cells was ~38% in WT cells and ~25% in *SPC42 SPC29* OE cells (Fig. 7 C, red-encircled numbers). After α-factor washout, the NPC occupancy at the distal end of the bridge increased to ~53% with the presence of the fusion SPB and climbed even higher to ~71% as the Spc42–Spc29 layer inserted into the NE. NPC occupancy dropped to ~10% after the fusion SPB had been completely inserted. In contrast, mSPBs rarely associated with NPCs (Fig. 7 C). These data suggest a mechanism of active recruitment of NPCs to the inserting SPB.

We applied SIM to follow NPCs during SPB duplication in WT cells. We synchronized *SPC42-yeGFP NIC96-tdTomato* cells with α-factor and analyzed NPC localization before and after release from the pheromone block. We determined the number of NPCs within a 100-nm radius to the mSPB (bright signal) and satellite/dSPB. The NPC occupancy at satellites in α-factor–arrested cells was ~40%. This number rose to ~60% with the insertion of the new SPB into the NE 20 min after α-factor washout (Fig. 7 D). At later time points, the NPC occupancy of the dSPB (SPB opposite to bud; Pereira et al., 2001) dropped to ~20%. During the course of the experiment, only 20–30% of mSPBs were associated with an NPC signal. Collectively, these data reflect the EM analysis in Fig. 7 C to suggest recruitment of an NPC to the inserting SPB.

NPCs are important for the insertion of the SPB into the NE

To analyze the function of this SPB-associated NPC for SPB duplication, we applied two strategies that were designed to rapidly inactivate NPCs in order to exclude secondary phenotypes that may arise from NPC defects. First, we used the auxin degron system (Nishimura et al., 2009) to inactivate NPCs before analyzing the impact of this NPC destruction upon SPB duplication. The combination of Nup188 and Nup133 auxin-mediated depletion was toxic for cells, as indicated by reduced growth (Fig. 8 A). Although Nup133-3HA-AID was rapidly depleted after auxin induction, Nup188-3HA-AID destruction took longer (Fig. 8 B). We partially degraded AID-tagged Nup188 and Nup133 for 1 h through the addition of auxin to α-factor–arrested cells (Fig. 8 C, timeline). Upon α-factor washout, SPB duplication was followed by monitoring the separation of two Spc42-mCherry signals and the incorporation of Spc110-yeGFP as markers of the consecutive stages of SPB duplication. Splitting of the Spc42-mCherry signals indicated that SPBs separated later in NPC-deprived cells (Fig. 8 C, left, red line) than in solvent control cells (black line) or control cells lacking the *NPC-AID* tag treated with auxin (gray line). The SPB-splitting delay in *NPC-AID* cells with auxin was likely caused by an SPB insertion defect because Spc110-yeGFP incorporated more slowly into the SPB of auxin-treated *NPC-AID* cells than into the SPBs of solvent control *NPC-AID* cells (Fig. 8 C, right).

Next, we assessed the ability of the Spc42 obelisk to embed within the NE of *NPC-AID SPC42* OE cells. In this experimental regimen (Fig. 8 D, timeline), the Spc42 obelisk can insert into the opening of the mSPB after forming a fusion SPB or next to the distal bridge end that contains the NPC. In the first scenario, we did not expect to see any delay in Spc110-yeGFP incorporation, even when NPCs were impaired. Indeed, Spc110-yeGFP accumulated at fusion SPBs with equal timing in solvent control and auxin-treated *NPC-AID* cells (Fig. 8 D, left). In contrast, in cells in which the Spc110-yeGFP SPB signal split during the experiment (Fig. 8 D, right; 40 and 55 min), and therefore the dSPB was inserted via the "normal" pathway, the dSPB showed a delay in Spc110-yeGFP incorporation when auxin was added in comparison with the solvent control (Fig. 8 D, right).

Second, we marked two NPC components with a triple-yeGFP (3GFP) and induced cross-linking of NPCs through the expression of a GFP-binding protein (GBP; Rothbauer et al., 2008) fused with the β-galactosidase gene *LacZ*. Because β-galactosidase is a tetramer (Jacobson et al., 1994), the GBP–β-galactosidase–GBP fusion protein was ideally suited to cross-link GFP-tagged NPCs, thereby sequestering them away from the SPB (Fig. 9 A). Galactose-induced expression of pGal1-*GBP–LacZ–GBP* reduced colony size of *NIC96-3GFP* and *NIC96-3GFP NUP133-3GFP* cells but had no impact on the growth of cells with OE of *3GBP* or the empty vector control (Fig. 9 B). OE of 3GBP and GBP–β-galactosidase–GBP was verified by immunoblotting (Fig. 9 C). GBP–β-galactosidase–GBP expression in α-factor–synchronized *NIC96-3GFP NUP133-3GFP* cells delayed SPB separation in a fraction of cells in comparison with the *NIC96-3GFP NUP133-3GFP* pGal1 control cells. This inhibition was more pronounced when
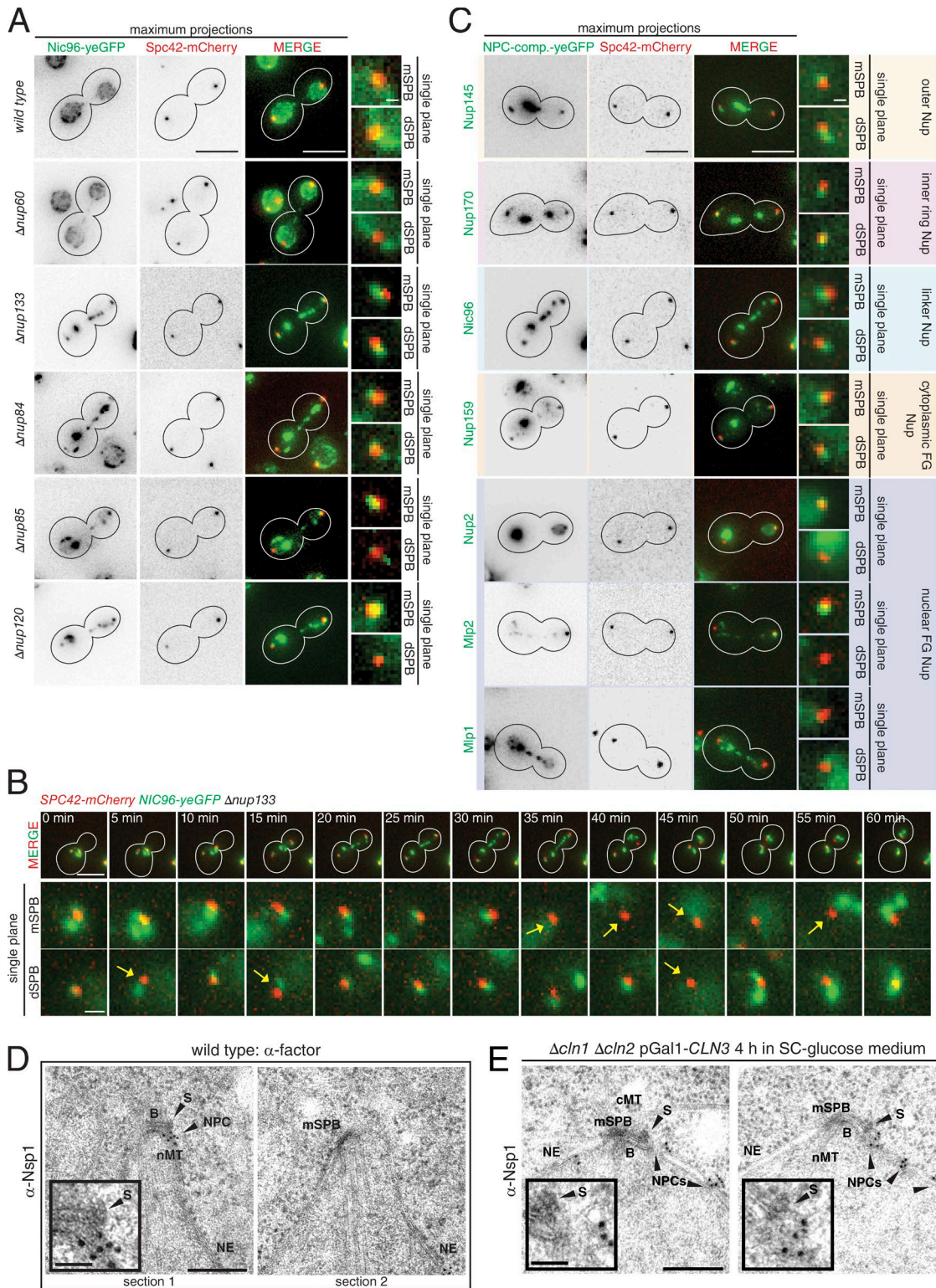
Figure 6. **NPC cluster mutant analysis and Nsp1 immuno-EM.** (A) *NIC96-yeGFP SPC42-mCherry* cells were analyzed in NPC cluster mutant cells. Representative images from live-cell microscopy are shown in the maximum projection and an SPB enlargement in single plane. Bars: (main images) 5 µm; (insets) 500 nm. (B) Live-cell microscopy of the *NIC96-yeGFP SPC42-mCherry Δnup133* cell from A. Arrows indicate times of no colocalization of SPB and NPC clusters. Bars: (main images) 5 µm; (insets) 1 µm. (C) *SPC42-mCherry Δnup133* were tagged with *NPC-yeGFP* to analyze the occupancy of NPC subclusters close to the SPB. Bars: (main images) 5 µm; (insets) 500 nm. FG, phenylalanine-glycine repeat; Nup, nucleoporin. (D and E) Immuno-EM analysis with α-Nsp1 antibody of WT cells arrested with α-factor (D) and *cln1,2Δ* pGal1-*CLN3*–depleted G1-arrested cells (E). Note that the bridge in D with the satellite and the anti-Nsp1 NPC signal is shown in the first serial section; the mSPB was detected in the second serial section. Bars: (main images) 200 nm; (insets) 50 nm. B, bridge; cMT, cytoplasmic MT; nMT, nuclear MT; S, satellite.
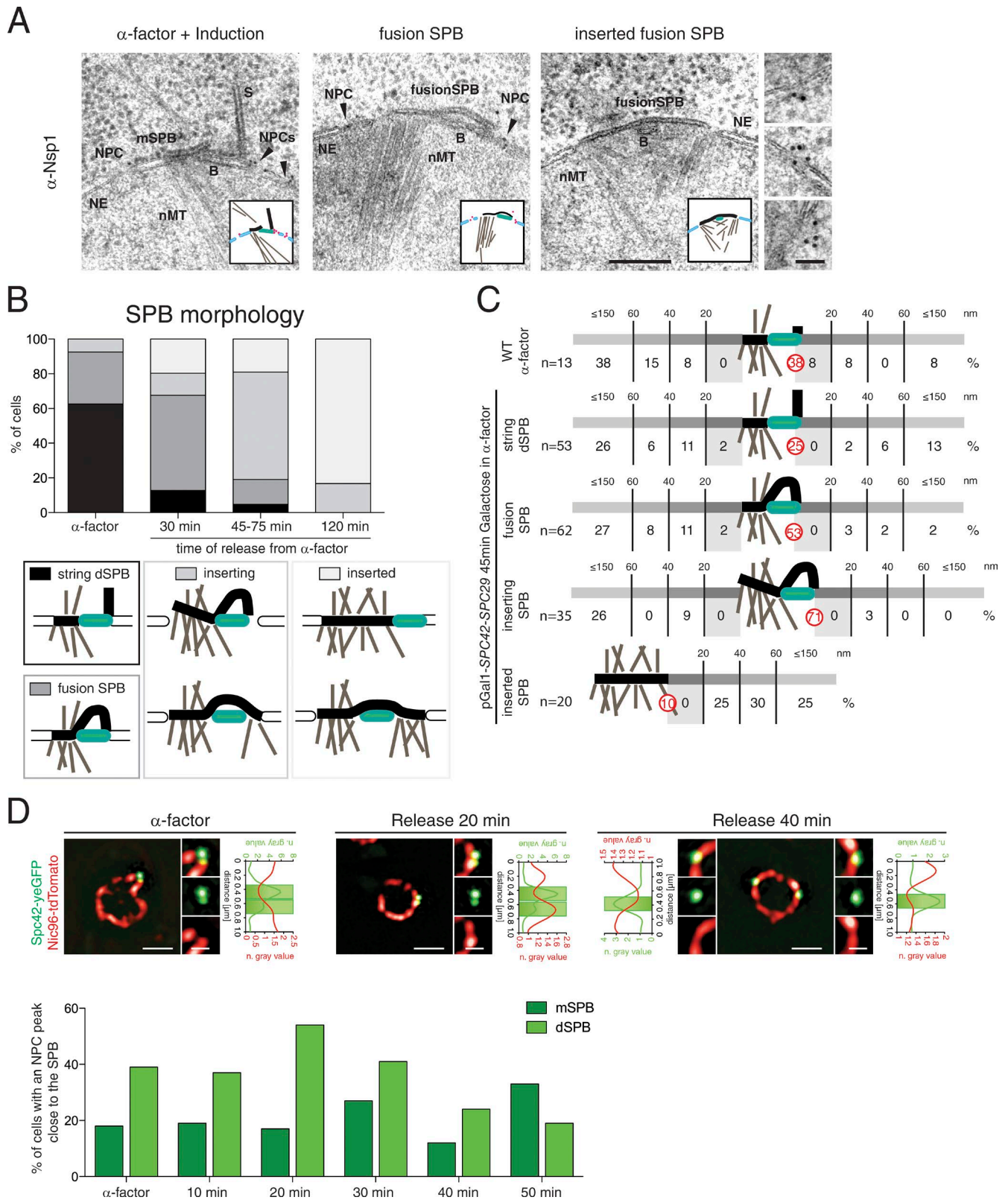
Figure 7. **Localization of NPCs in proximity to duplicating SPBs.** (A) Immuno-EM analysis with α-Nsp1 antibody of *SPC42 SPC29* OE cells with 45 min induction during α-factor arrest and after release into the cell cycle. EM enlargements on the right show NPCs labeled by the α-Nsp1 antibody from the NE of the "inserted fusion SPB" cell. Cartoons illustrate SPB phenotypes and gold particles (pink). B, bridge; N, nucleus; nMT, nuclear MT; S, satellite. Bars: (main images) 200 nm; (insets) 50 nm. (B) Phenotype analysis of EM images (Figs. 1, 2, and 3). n > 100 for the entire dataset. (C) Quantification of EM micrographs categorized according to their phenotypes and analyzed for the distance between the mSPB/satellite and NPCs. In the three bottom categories, the G1 block was released. n, number of analyzed SPBs. Red-encircled numbers indicate NPCs (%) at the distal end of the bridge. (D) Representative images and quantification of SIM analysis in *SPC42-yeGFP NIC96-tdTomato* WT cells in α-factor arrest and upon release. n ≥ 30. Bars: (main images) 2 μm; (insets) 500 nm.
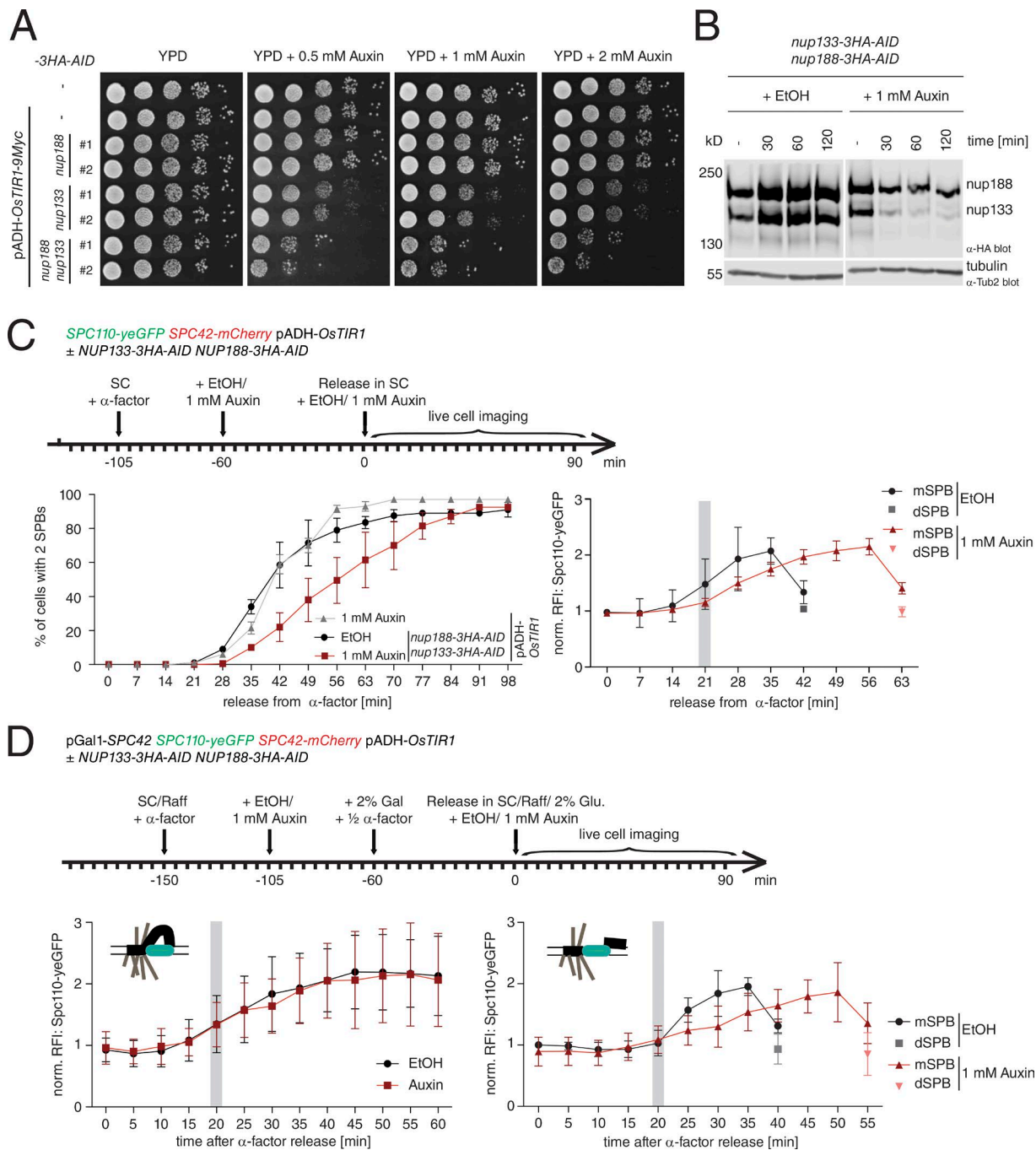
Figure 8. **NPC auxin depletion experiment.** (A) Growth of strains. (B) Western blot after treatment with EtOH or 1 mM auxin. Tubulin was used as a loading control. (C, top) Experimental design. (Left) SPB splitting was analyzed based on Spc42-mCherry signal. Two independent experiments. $n > 50$. (Right) Spc110-yeGFP recruitment was quantified to measure the time of dSPB NE insertion. The gray bar indicates budding. mSPBs and dSPBs were quantified separately after their separation (42 and 63 min). $n > 20$. (D, top) Outline of experiment. Spc110-yeGFP recruitment was analyzed in cells with SPB fusion (left) and cells with splitting SPBs (right). Gray bars indicate time of budding. (Right) The signals of the mSPB and dSPB are indicated after SPB separation in the right graph (40 and 55 min). $n > 50$ (left) and ≥ 20 (right). Error bars indicate SD. RFI, reflective fluorescence intensity.

the duration of *GBP–LacZ–GBP* OE was extended to 90 min (Fig. 9 D). Interestingly, even after 60 min release, 30–50% of pGal1-*GBP–LacZ–GBP NIC96-3GFP NUP133-3GFP* cells failed to separate the SPBs, whereas the number unable to do this in pGal1 control cultures was lower (Fig. 9 D, right).

To gain better insights into the SPB duplication defect in *NPC-3GFP* pGal1-*GBP–LacZ–GBP* cells, we analyzed SPB duplication in relation with NPC localization by live-cell microscopy. *NIC96-3GFP NUP133-3GFP* cells containing the pGal1 control plasmid had equally distributed NPCs along the NE, and the red Spc42-mCherry SPB marker was closely associated with NPCs during SPB separation (Fig. 9 E). *NIC96-3GFP NUP133-3GFP GBP–LacZ–GBP* cells that separated the SPBs early had NPC clusters close to the SPB (Fig. 9 E, "normal separation"). Cells with delayed or no separation of SPBs had SPBs that were either only transiently associated with NPC
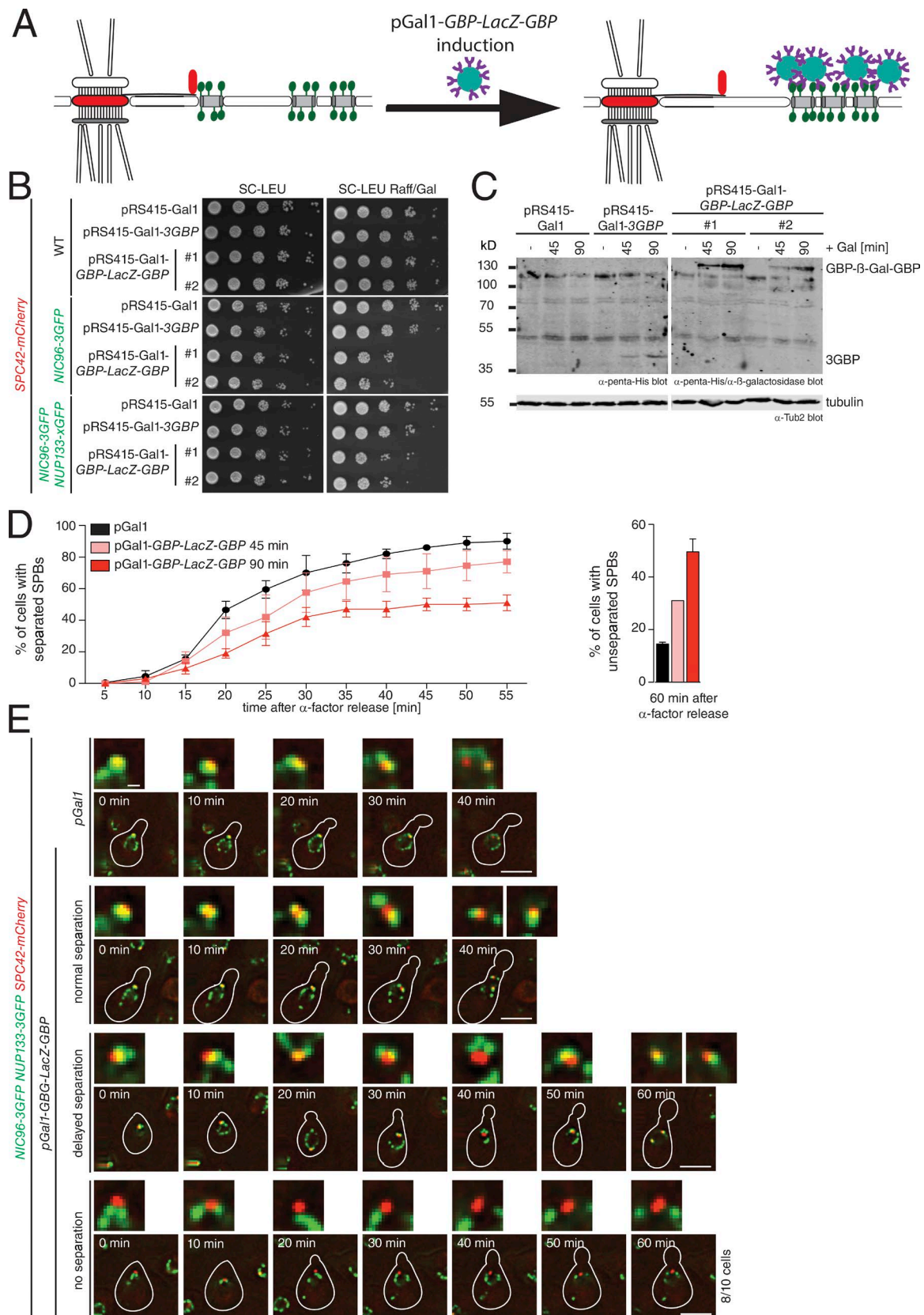
Figure 9. **NPC clustering.** (A) Model showing how cells were arrested with α-factor followed by GBP–β-galactosidase–GBP cross-links of NPCs. (B) Drop test of strains (10-fold serial dilutions). LEU, leucin. (C) Western blot analysis to confirm construct expression. (D) Quantification of the SPB splitting in cells overexpressing *GBP–LacZ–GBP* for 45 min or 90 min in α-factor–arrested cells normalized to budding (*t* = 0). At least two individual experiments. Error bars indicate SD. *n* ≥ 50. (E) Exemplarily single-stack live-cell images of cells in D. Normal separation (40 min), delayed separation (60 min), and no separation are shown. Bars: (main images) 5 µm; (insets) 500 nm.

clusters or not associated with the clusters at all, respectively (Fig. 9 E, "delayed separation" or "no separation"). This correlation suggests that the recruitment of NPCs to SPBs as seen in Fig. 7 is important for SPB duplication and insertion.

Discussion

Like their metazoan counterpart the centrosome, SPBs duplicate once per cell cycle. The preexisting mSPB provides a platform for the assembly of the daughter. However, the bridge structure separates the satellite from the mSPB by 120 nm (Byers and Goetsch, 1975; Li et al., 2006). The functional significance of this spacing has remained unclear. In this study, we provide evidence that in G1 phase and mitosis, the Spc42 polymer has fusogenic properties that may be important for SPB fusion during karyogamy (Byers and Goetsch, 1975; Melloy et al., 2007; Gibeaux et al., 2013). However, this fusion has to be prevented during the SPB duplication of cycling cells to ensure bipolar spindle formation.

The satellite is a miniature version of the cytoplasmic side of the mSPB. It has been described as a spherical structure anchored at the distal end of the bridge (Byers and Goetsch, 1975). Satellite extension into an obelisk by *SPC42* OE suggests that the Spc42 layer in the satellite is angled by 45–90° relative to the NE. EM analysis confirmed the elongated and angled nature of the satellite in WT cells. Similar observations have been made in nonsynchronized diploid cells (O'Toole et al., 1999). The fact that the satellite only expanded outwards of the NE suggests that its Spc42 layer is blocked at the NE side, probably because of anchorage to the bridge and/or the NE.

The polar and angled nature of the satellite might have important implications for mating and SPB duplication. First, the upright orientation of the satellite might favor the SPB fusion step during karyogamy (Byers and Goetsch, 1975; Melloy et al., 2007). Second, when considered alongside the angled positioning of the DP during NE insertion (Adams and Kilmartin, 1999), this incorporation of Spc42 into the distal end of the satellite probably means that the DP either has to rotate after or during its expansion, as we observed for the Spc42 obelisk, or it must detach from the bridge and then insert into the NE leading with its proximal end.

The phenotype of conditional lethal *spc110* mutants with mutations in the conserved C-terminal pericentrin–AKAP450 centrosomal targeting (PACT) domain, which is important for the interaction with the central plaque (Kilmartin and Goh, 1996; Stirling et al., 1996; Sundberg and Davis, 1997), suggests an inserting role of the binding of the Spc110 from within the nucleus to the Spc42–Spc29 layer of the DP during insertion (Elliott et al., 1999). As soon as the SPB is inserted into the NE, the SPIN proteins Bbp1-Mps2, Nbp1, and Ndc1 surrounded the central Spc42 layer. This is consistent with the appearance of Ndc1 and Bbp1-Mps2 rings in tetraploid yeast cells around the enlarged SPBs (Burns et al., 2015). However, our data suggest that the SPIN component rings only assemble with the insertion of the new SPB into the NE and that these rings may be flexible and adapt to the size of the central Spc42 polymer. They may therefore not form a pore into which the new SPB inserts. Rather, they probably help to embed the SPB into the NE by providing an interface between the Spc42 polymer of the central plaque and the lipid bilayer. Such an embedding function is suggested

from the analysis of conditional lethal SPIN mutants in the presence of *SPC42 SPC29* OE.

Our exclusion of DP growth as an essential driving force for NE insertion raises the question of how the SPB inserts into the NE. In this study, we show that an NPC becomes recruited specifically to the developing dSPB during the time of NE insertion. Degradation of NPC components through exploitation of the auxin degron system affected the timing of SPB insertion into the NE. Further confirmation of a role for the NPC in SPB duplication emerged from experiments in which we expressed a *GBP–LacZ–GBP* fusion in *NIC96/NUP133-3GFP*–tagged cells to induce NPC clustering. This clustering-delayed SPB duplication depended on the localization of the cluster. Only SPBs that were not associated with NPCs had a duplication defect. There remains the possibility that such NPC manipulations affect SPB insertion indirectly because of alterations in NE composition/structure. However, several findings argue in favor of a direct role of NPCs. First, insertion of the fusion SPB via the mSPB NE opening was unaffected upon NPC auxin depletion. Second, the kinetics of Spc110 incorporation in the very same experiment was the same in *NPC-AID* cells with solvent control or auxin, indicating that auxin-treated cells had sufficient Spc110 complexes within the nucleus to insert the SPB into the NE (Elliott et al., 1999). Third, the SPB duplication defect was more pronounced when the NPC cluster did not localize to the SPB, indicating that an NPC in the vicinity of the SPB is needed for efficient duplication. Fourth, it was reported that the NPC-associated protein Mlp2 has a function in SPB assembly (Niepel et al., 2005). Finally, the essential functions of *MPS2* and *MPS3* during SPB duplication are suppressed by deletion of the NPC components *POM152*, *POM34*, or *MPL1/2* (Sezen et al., 2009; Witkin et al., 2010). These data collectively suggest that NPCs have an active role in SPB duplication. This SPB-associated NPC pool may assist the insertion of the new SPB into the NE by providing an opening in the NE, or it may deliver duplication factors such as Ndc1 to the insertion site. Further analyses are required to discriminate these possibilities.

Materials and methods

Yeast strains, plasmids, and culture conditions

All yeast strains are derived from ESM356-1 (*MATa ura3-52 trp1Δ63 his3Δ200 leu2Δ1*) and ESM357-9 (*MATα ura3-52 trp1Δ63 his3Δ200 leu2Δ1*) and are listed in Table S1, including all plasmids used in this study. Endogenous gene tagging and gene deletions were performed using previously described PCR-based methods (Knop et al., 1999; Janke et al., 2004). Tagging was verified by microscopy and via colony PCR. Yeast strains were grown in synthetic complete (SC) medium, low-fluorescence medium (SC medium prepared with yeast nitrogen base lacking folic acid and riboflavin; Sheff and Thorn, 2004), SC-raffinose (SC-Raf), or YP-Raf (yeast extract, peptone, and raffinose) at 23°C, 30°C, or 35°C. Nocodazole was used at a final concentration of 15 µg/ml in SC medium supplemented with 1% peptone. Galactose was added to a final concentration of 2% to induce expression of genes under a pGal1 promoter in cells grown in YP-Raf or SC-Raf. In contrast, the addition of 2% glucose represses pGal1 gene expression. For G1 synchronization, 10 µg/ml α-factor was added to the cell culture for the indicated time span. To sustain an extended G1 arrest, α-factor was re-added with a concentration of 5 µg/ml (1/2 α-factor). To release the cells back into cell cycle, the culture was washed three times with α-factor–free medium. To analyze protein level by Western blot, we used alkaline lysis

and TCA to prepare total yeast protein extract (Knop et al., 1999). To generate zygotes, log-phase haploid strains were mixed in low-fluorescence medium for 3.5 h before imaging began. To test for cellular fitness, yeast cells were grown overnight in liquid culture before the density was adjusted to $OD_{600} = 1$ the next day. The cell suspension was then spotted in a 10-fold serial dilution on the desired plates and incubated at the indicated temperatures. For generation of temperature-sensitive (ts) strains, we followed the synthetic genetic array analysis–compatible strategy published by Li et al. (2011). Therefore, all ts mutants were integrated in their native loci and selected with the KanMX4 marker.

Statistical analysis

Data were analyzed using two-tailed *t* tests. Data distribution was assumed to be normal, but this was not formally tested.

Fluorescence light microscopy

For live-cell imaging, a DeltaVision RT system (Olympus IX71 based; Applied Precision Ltd.) equipped with a Photometrics CoolSnap HQ camera (Roper Scientific), 100× 1.4 NA Super–Plan Apochromat and 60× 1.42 NA Plan Apochromat oil objectives (Olympus), a four-color Standard InsightSSI module light source including a laser-based hardware autofocus, and Workstation with a CentOS operating system and SoftWoRx software (Applied Precision Ltd.) was used. The imaging was performed at 23°C, 30°C, or 35°C within the system enclosures. The cells were immobilized on Concanavalin A (Sigma-Aldrich)–coated 35-mm glass bottomed dishes (P35G-1.5-14C; MatTek Corporation) and kept in their respective media. To compare fluorescence intensities, all quantification experiments were conducted at the same exposure and illumination settings, the 100× objective, and a 2 × 2 binning. Image processing and analysis was performed semiautomated with the open-source ImageJ 1.46r software package (National Institutes of Health). For quantification, the integrated density (IntDen) of the SPB in the brightest stack was measured with 5 × 5 and 7 × 7 squares for background correction. The following formula was used to calculate the relative fluorescent intensity (RFI): $RFI = IntDen_{5 \times 5} - ([IntDen_{7 \times 7} - IntDen_{5 \times 5}] \times [area_{5 \times 5} / \{area_{7 \times 7} - area_{5 \times 5}\}])$. Quantifications were performed two to three times, and either a representative experiment or a combined graph is shown.

SIM

For SIM analysis, cells were fixed in the desired cell state for 15 min in 4% paraformaldehyde/2% sucrose in PBS solution and washed extensively with PBS. Cells were placed on a glass-bottomed dish as described in the previous section and were kept for the time of imaging in PBS. The samples were imaged on a Nikon N-SIM system equipped with total internal reflection fluorescence Apochromat 100× 1.49 NA oil immersion objective and a single photon–detection electron-multiplying charge-coupled device camera (iXon3 DU-897E; Andor Technology). 488- and 561-nm laser lines were used for excitation of yeGFP and tdTomato/mCherry, respectively, combined with emission band pass filter 520/45 and 610/60. Images were taken sequentially within a small z stack and in consideration to image SPBs close to the coverslip to minimize spherical aberrations. Subsequently, the reconstruction and channel alignment and FWHM measurements were performed with the NIS imaging and image analysis software (Nikon). For the xyz chromatic shift correction, a reference sample with tetraspeck beads was used. Images always show a single stack of the z slices. For the proximity analysis of NPCs close to the mSPB or satellite/dSPB, plot profiles were generated. Signals within a 200-nm diameter around the yeGFP signal peak were counted as colocalizations.

FRET

For FRET analysis of fluorescent protein–labeled Spc42 zygotes, a DeltaVision Elite widefield fluorescence microscope (GE Healthcare) consisting of an inverted epifluorescence microscope (IX71; Olympus) equipped with a light-emitting diode light engine (seven-color InsightSSI module; GE Healthcare), an sCMOS camera (pco.edge 4.2; PCO), and a 60× 1.42 NA Plan Apochromat N oil immersion objective (Olympus) was used. Imaging was performed at 30°C with cells immobilized in glass-bottomed 96-well plates (MGB096-1-2-LG-L; Matrical) using Concanavalin A as described previously (Khmelinskii and Knop, 2014). Emission from mTurquoise and eYFP was recorded using z stacks of 16 planes with 0.3-µm spacing by detecting the fluorescence from 458–482 and 540–578 nm, respectively, before and after accepter photobleaching. For accepter photobleaching of eYFP, an irradiation using the InsightSSI module light source with a light of wavelength of 505–515 nm was used for 40 s. Image quantification was performed in ImageJ using maximum-intensity z projections of the image stacks. For quantification, a circle with a diameter of 8 pixels was placed around the SPB and in proximity to the SPB within the same cell for background correction. The mean intensities within these selections were measured, and the cellular background intensity was subtracted from the intensity of the SPB (Muller et al., 2005). The FRET efficiency between mTurquoise and eYFP was calculated as the percent increase of background-corrected integrated pixel intensity of the donor mTurquoise after accepter photobleaching according to the equation:

$$FRET\ efficiency = \frac{INTENSITY\ donor\ post - INTENSITY\ donor\ pre}{INTENSITY\ donor\ post}.$$

Finally the FRET efficiency was normalized by multiplying with the median of background-corrected mean intensity of SPBs of the donor-only control strain (Gryaznova et al., 2016).

EM

Cells were high-pressure frozen, freeze-substituted, sectioned, labeled, and stained for EM as described (Giddings et al., 2001). In brief, cells were collected onto a 0.45-µm polycarbonate filter (EMD Millipore) using vacuum filtration and then were high-pressure frozen with an HPM010 (Abra-Fluid). Cells were freeze-substituted using the EM-AFS2 device (freeze substitution solution: 0.1% glutaraldehyde, 0.2% uranyl acetate, and 1% water [dissolved in anhydrous acetone]; Leica Microsystems) and stepwise infiltrated with Lowicryl HM20 (Polysciences, Inc.) started by a low temperature of −90°C. For polymerization, the samples were finally exposed to UV light for 48 h at −45°C and were gradually warmed up to 20°C. Embedded cells were serially sectioned using a Reichert Ultracut S Microtome (Leica Instruments) to a thickness of 70 nm. Poststaining with 2% uranyl acetate and lead citrate was performed. The sections were imaged with an electron microscope (CM120 BioTwin; Philips Electronics N.V.) operated at 80–100 kV and equipped with a charge-coupled device camera (Keen View; Soft Imaging Systems) or were imaged with a transmission electron microscope (JE-1400, JEOL) operating at 80 kV equipped with a 4,000 × 4,000 digital camera (F416; TVIPS). Micrographs were adjusted in brightness and contrast using ImageJ. For immunolabeling, primary antibodies were used against GFP, Spc42, and Nsp1. The samples were prepared similarly, with the exception that the glutaraldehyde was omitted from the freeze-substitution solution. The sections were treated with blocking buffer (1.5% BSA and 0.1% fish skin gelatin in PBS) and then incubated with the primary antibodies followed by treatment with protein A–gold conjugates (10 nm; Utrecht University).

Antibodies

Antibodies and their conditions of use are mentioned as follows: mouse anti-Nsp1 (immuno-EM; 1:100; ab4641; Abcam), rabbit anti-GFP (immuno-EM; 1:5; provided by M. Seedorf, Zentrum für Molekulare Biologie, Heidelberg, Germany), mouse anti-GFP (Western blot; 1:1,000; 11814460-001; Roche), rabbit anti-Spc42 (immuno-EM; 1:100; Western blot, 1:1,000; Elliott et al., 1999), rabbit anti-Spc29 (Western blot; 1:1,000; Elliott et al., 1999), rat anti-HA (Western blot; 1:1,000; 1867423; Boehringer), mouse anti-His (Western blot; 1:1,000; 34660; QIAGEN), and rabbit anti-Tub2 (Western blot; 1:1,000; Elliott et al., 1999).

Online supplemental material

Fig. S1 shows characterization of strains and Spc29, Spc42, and *CLN*-deletion mutant cells. Fig. S2 shows Mps2 localization and nocodazole SPB fusion experiments. Fig. S3 shows localization of SPIN components. Fig. S4 shows analysis of SPB ts mutant cells. Table S1 lists all the strains and plasmids used in the study.

References

Adams, I.R., and J.V. Kilmartin. 1999. Localization of core spindle pole body (SPB) components during SPB duplication in *Saccharomyces cerevisiae*. *J. Cell Biol.* 145:809–823. http://dx.doi.org/10.1083/jcb.145.4.809

Araki, Y., C.K. Lau, H. Maekawa, S.L. Jaspersen, T.H. Giddings Jr., E. Schiebel, and M. Winey. 2006. The *Saccharomyces cerevisiae* spindle pole body (SPB) component Nbp1p is required for SPB membrane insertion and interacts with the integral membrane proteins Ndc1p and Mps2p. *Mol. Biol. Cell.* 17:1959–1970. http://dx.doi.org/10.1091/mbc.E05-07-0668

Bullitt, E., M.P. Rout, J.V. Kilmartin, and C.W. Akey. 1997. The yeast spindle pole body is assembled around a central crystal of Spc42p. *Cell.* 89:1077–1086. http://dx.doi.org/10.1016/S0092-8674(00)80295-0

Burns, S., J.S. Avena, J.R. Unruh, Z. Yu, S.E. Smith, B.D. Slaughter, M. Winey, and S.L. Jaspersen. 2015. Structured illumination with particle averaging reveals novel roles for yeast centrosome components during duplication. *eLife.* 4:e08586. http://dx.doi.org/10.7554/eLife.08586

Byers, B. 1981a. Multiple roles of the spindle pole bodies in the life cycle of Saccharomyces cerevisiae. *In* Molecular Genetics in Yeast. Vol. 16. D. Wettstein, A. Stenderup, M. Kielland-Brandt, and J. Friis, editors. Alfred Benzon Symp., Munksgaard, Copenhagen. 119-133.

Byers, B., and L. Goetsch. 1975. Behavior of spindles and spindle plaques in the cell cycle and conjugation of *Saccharomyces cerevisiae*. *J. Bacteriol.* 124:511–523.

Denning, D., B. Mykytka, N.P. Allen, L. Huang, Al Burlingame, and M. Rexach. 2001. The nucleoporin Nup60p functions as a Gsp1p–GTP-sensitive tether for Nup2p at the nuclear pore complex. *J. Cell Biol.* 154:937–950. http://dx.doi.org/10.1083/jcb.200101007

Donaldson, A.D., and J.V. Kilmartin. 1996. Spc42p: A phosphorylated component of the *S. cerevisiae* spindle pole body (SPD) with an essential function during SPB duplication. *J. Cell Biol.* 132:887–901. http://dx.doi.org/10.1083/jcb.132.5.887

Elliott, S., M. Knop, G. Schlenstedt, and E. Schiebel. 1999. Spc29p is a component of the Spc110p subcomplex and is essential for spindle pole body duplication. *Proc. Natl. Acad. Sci. USA.* 96:6205–6210. http://dx.doi.org/10.1073/pnas.96.11.6205

Gibeaux, R., A.Z. Politi, F. Nédélec, C. Antony, and M. Knop. 2013. Spindle pole body-anchored Kar3 drives the nucleus along microtubules from another nucleus in preparation for nuclear fusion during yeast karyogamy. *Genes Dev.* 27:335–349. http://dx.doi.org/10.1101/gad.206318.112

Giddings, T.H. Jr., E.T. O'Toole, M. Morphew, D.N. Mastronarde, J.R. McIntosh, and M. Winey. 2001. Using rapid freeze and freeze-substitution for the preparation of yeast cells for electron microscopy and three-dimensional analysis. *Methods Cell Biol.* 67:27–42. http://dx.doi.org/10.1016/S0091-679X(01)67003-1

Grandi, P., N. Schlaich, H. Tekotte, and E.C. Hurt. 1995. Functional interaction of Nic96p with a core nucleoporin complex consisting of Nsp1p, Nup49p and a novel protein Nup57p. *EMBO J.* 14:76–87.

Gruneberg, U., K. Campbell, C. Simpson, J. Grindlay, and E. Schiebel. 2000. Nud1p links astral microtubule organization and the control of exit from mitosis. *EMBO J.* 19:6475–6488. http://dx.doi.org/10.1093/emboj/19.23.6475

Gryaznova, Y., A. Koca Caydasi, G. Malengo, V. Sourjik, and G. Pereira. 2016. A FRET-based study reveals site-specific regulation of spindle position checkpoint proteins at yeast centrosomes. *eLife.* 5:e14029. http://dx.doi.org/10.7554/eLife.14029

Jacobs, C.W., A.E.M. Adams, P.J. Szaniszlo, and J.R. Pringle. 1988. Functions of microtubules in the *Saccharomyces cerevisiae* cell cycle. *J. Cell Biol.* 107:1409–1426. http://dx.doi.org/10.1083/jcb.107.4.1409

Jacobson, R.H., X.J. Zhang, R.F. DuBose, and B.W. Matthews. 1994. Three-dimensional structure of β-galactosidase from *E. coli.* *Nature.* 369:761–766. http://dx.doi.org/10.1038/369761a0

Janke, C., M.M. Magiera, N. Rathfelder, C. Taxis, S. Reber, H. Maekawa, A. Moreno-Borchart, G. Doenges, E. Schwob, E. Schiebel, and M. Knop. 2004. A versatile toolbox for PCR-based tagging of yeast genes: new fluorescent proteins, more markers and promoter substitution cassettes. *Yeast.* 21:947–962. http://dx.doi.org/10.1002/yea.1142

Jaspersen, S.L., and M. Winey. 2004. The budding yeast spindle pole body: Structure, duplication, and function. *Annu. Rev. Cell Dev. Biol.* 20:1–28. http://dx.doi.org/10.1146/annurev.cellbio.20.022003.114106

Jeoung, D.I., L.J. Oehlen, and F.R. Cross. 1998. Cln3-associated kinase activity in *Saccharomyces cerevisiae* is regulated by the mating factor pathway. *Mol. Cell. Biol.* 18:433–441. http://dx.doi.org/10.1128/MCB.18.1.433

Khmelinskii, A., and M. Knop. 2014. Analysis of protein dynamics with tandem fluorescent protein timers. *Methods Mol. Biol.* 1174:195–210. http://dx.doi.org/10.1007/978-1-4939-0944-5_13

Kilmartin, J.V. 2003. Sfi1p has conserved centrin-binding sites and an essential function in budding yeast spindle pole body duplication. *J. Cell Biol.* 162:1211–1221. http://dx.doi.org/10.1083/jcb.200307064

Kilmartin, J.V. 2014. Lessons from yeast: the spindle pole body and the centrosome. *Philos. Trans. R. Soc. Lond. B Biol. Sci.* 369:20130456. http://dx.doi.org/10.1098/rstb.2013.0456

Kilmartin, J.V., and P.Y. Goh. 1996. Spc110p: assembly properties and role in the connection of nuclear microtubules to the yeast spindle pole body. *EMBO J.* 15:4592–4602.

Kilmartin, J.V., S.L. Dyos, D. Kershaw, and J.T. Finch. 1993. A spacer protein in the *Saccharomyces cerevisiae* spindle poly body whose transcript is cell cycle-regulated. *J. Cell Biol.* 123:1175–1184. http://dx.doi.org/10.1083/jcb.123.5.1175

Knop, M., K. Siegers, G. Pereira, W. Zachariae, B. Winsor, K. Nasmyth, and E. Schiebel. 1999. Epitope tagging of yeast genes using a PCR-based strategy: more tags and improved practical routines. *Yeast.* 15(10B):963–972. http://dx.doi.org/10.1002/(SICI)1097-0061(199907)15:10B<963::AID-YEA399>3.0.CO;2-W

Kurihara, L.J., C.T. Beh, M. Latterich, R. Schekman, and M.D. Rose. 1994. Nuclear congression and membrane fusion: two distinct events in the yeast karyogamy pathway. *J. Cell Biol.* 126:911–923. http://dx.doi.org/10.1083/jcb.126.4.911

Li, S., A.M. Sandercock, P. Conduit, C.V. Robinson, R.L. Williams, and J.V. Kilmartin. 2006. Structural role of Sfi1p–centrin filaments in budding yeast spindle pole body duplication. *J. Cell Biol.* 173:867–877. http://dx.doi.org/10.1083/jcb.200603153

Li, Z., F.J. Vizeacoumar, S. Bahr, J. Li, J. Warringer, F.S. Vizeacoumar, R. Min, B. Vandersluis, J. Bellay, M. Devit, et al. 2011. Systematic exploration of essential yeast gene function with temperature-sensitive mutants. *Nat. Biotechnol.* 29:361–367. http://dx.doi.org/10.1038/nbt.1832

Melloy, P., S. Shen, E. White, J.R. McIntosh, and M.D. Rose. 2007. Nuclear fusion during yeast mating occurs by a three-step pathway. *J. Cell Biol.* 179:659–670. http://dx.doi.org/10.1083/jcb.200706151

Muller, E.G., B.E. Snydsman, I. Novik, D.W. Hailey, D.R. Gestaut, C.A. Niemann, E.T. O'Toole, T.H.J. Giddings Jr., B.A. Sundin, and T.N. Davis. 2005. The organization of the core proteins of the yeast spindle pole body. *Mol. Biol. Cell.* 16:3341–3352. http://dx.doi.org/10.1091/mbc.E05-03-0214

Niepel, M., C. Strambio-de-Castillia, J. Fasolo, B.T. Chait, and M.P. Rout. 2005. The nuclear pore complex–associated protein, Mlp2p, binds to the yeast spindle pole body and promotes its efficient assembly. *J. Cell Biol.* 170:225–235. http://dx.doi.org/10.1083/jcb.200504140

Nishimura, K., T. Fukagawa, H. Takisawa, T. Kakimoto, and M. Kanemaki. 2009. An auxin-based degron system for the rapid depletion of proteins in nonplant cells. *Nat. Methods.* 6:917–922. http://dx.doi.org/10.1038/nmeth.1401

O'Toole, E.T., M. Winey, and J.R. McIntosh. 1999. High-voltage electron tomography of spindle pole bodies and early mitotic spindles in the yeast *Saccharomyces cerevisiae. Mol. Biol. Cell.* 10:2017–2031. http://dx.doi.org/10.1091/mbc.10.6.2017

Otsuka, S., K.H. Bui, M. Schorb, M.J. Hossain, A.Z. Politi, B. Koch, M. Eltsov, M. Beck, and J. Ellenberg. 2016. Nuclear pore assembly proceeds by an inside-out extrusion of the nuclear envelope. *eLife.* 5:e19071. http://dx.doi.org/10.7554/eLife.19071

Pereira, G., T.U. Tanaka, K. Nasmyth, and E. Schiebel. 2001. Modes of spindle pole body inheritance and segregation of the Bfa1p–Bub2p checkpoint protein complex. *EMBO J.* 20:6359–6370. http://dx.doi.org/10.1093/emboj/20.22.6359

Rothbauer, U., K. Zolghadr, S. Muyldermans, A. Schepers, M.C. Cardoso, and H. Leonhardt. 2008. A versatile nanotrap for biochemical and functional studies with fluorescent fusion proteins. *Mol. Cell. Proteomics.* 7:282–289. http://dx.doi.org/10.1074/mcp.M700342-MCP200

Rout, M.P., and J.V. Kilmartin. 1990. Components of the yeast spindle and spindle pole body. *J. Cell Biol.* 111:1913–1927. http://dx.doi.org/10.1083/jcb.111.5.1913

Rüthnick, D., and E. Schiebel. 2016. Duplication of the yeast spindle pole body once per cell cycle. *Mol. Cell. Biol.* 36:1324–1331. http://dx.doi.org/10.1128/MCB.00048-16

Schaerer, F., G. Morgan, M. Winey, and P. Philippsen. 2001. Cnm67p is a spacer protein of the *Saccharomyces cerevisiae* spindle pole body outer plaque. *Mol. Biol. Cell.* 12:2519–2533. http://dx.doi.org/10.1091/mbc.12.8.2519

Seybold, C., M. Elserafy, D. Rüthnick, M. Ozboyaci, A. Neuner, B. Flottmann, M. Heilemann, R.C. Wade, and E. Schiebel. 2015. Kar1 binding to Sfi1 C-terminal regions anchors the SPB bridge to the nuclear envelope. *J. Cell Biol.* 209:843–861. http://dx.doi.org/10.1083/jcb.201412050

Sezen, B., M. Seedorf, and E. Schiebel. 2009. The SESA network links duplication of the yeast centrosome with the protein translation machinery. *Genes Dev.* 23:1559–1570. http://dx.doi.org/10.1101/gad.524209

Sheff, M.A., and K.S. Thorn. 2004. Optimized cassettes for fluorescent protein tagging in *Saccharomyces cerevisiae. Yeast.* 21:661–670. http://dx.doi.org/10.1002/yea.1130

Stirling, D.A., T.F. Rayner, A.R. Prescott, and M.J. Stark. 1996. Mutations which block the binding of calmodulin to Spc110p cause multiple mitotic defects. *J. Cell Sci.* 109:1297–1310.

Sundberg, H.A., and T.N. Davis. 1997. A mutational analysis identifies three functional regions of the spindle pole component Spc110p in *Saccharomyces cerevisiae. Mol. Biol. Cell.* 8:2575–2590. http://dx.doi.org/10.1091/mbc.8.12.2575

Wang, R., A. Kamgoue, C. Normand, I. Léger-Silvestre, T. Mangeat, and O. Gadal. 2016. High resolution microscopy reveals the nuclear shape of budding yeast during cell cycle and in various biological states. *J. Cell Sci.* 129:4480–4495.

Wente, S.R., and G. Blobel. 1994. NUP145 encodes a novel yeast glycine-leucine-phenylalanine-glycine (GLFG) nucleoporin required for nuclear envelope structure. *J. Cell Biol.* 125:955–969. http://dx.doi.org/10.1083/jcb.125.5.955

Winey, M., L. Goetsch, P. Baum, and B. Byers. 1991. *MPS1* and *MPS2*: novel yeast genes defining distinct steps of spindle pole body duplication. *J. Cell Biol.* 114:745–754. http://dx.doi.org/10.1083/jcb.114.4.745

Winey, M., D. Yarar, T.H. Giddings Jr., and D.N. Mastronarde. 1997. Nuclear pore complex number and distribution throughout the *Saccharomyces cerevisiae* cell cycle by three-dimensional reconstruction from electron micrographs of nuclear envelopes. *Mol. Biol. Cell.* 8:2119–2132. http://dx.doi.org/10.1091/mbc.8.11.2119

Witkin, K.L., J.M. Friederichs, O. Cohen-Fix, and S.L. Jaspersen. 2010. Changes in the nuclear envelope environment affect spindle pole body duplication in *Saccharomyces cerevisiae. Genetics.* 186:867–883. http://dx.doi.org/10.1534/genetics.110.119149